SIMULATION RESEARCH ON THE INDUCTION HEATING EFFECT OF LARGE–DIAMETER PIPELINES BASED ON MAXWELL AND WORKBENCH MULTI–FIELD COUPLING

Xiao-xiao ZHU [1, 2*], Chang-Xing DU[3], Hao-Yu LIU[4], Shi-Min ZHANG[5]

With the growth of large-diameter onshore pipeline construction, demand for mechanized anti-corrosion joint repair via heat-shrinkable sleeves rises. Induction heating, superior to inefficient, uneven manual gas torch heating, is key for quality. This study develops a multifunctional apparatus (rust removal, painting, induction heating) for 1016-mm pipelines. Maxwell simulations optimize heating distance—reducing it from 5 mm to 3 mm boosts thermal efficiency by 19.9%. Workbench simulations show pipelines reach over 200°C in 200s (initial temp -20°C to 22°C) with good adaptability. Heating at 5000 Hz yields 1.7 times the temperature of 3000 Hz, and 48 sampling points confirm temperature deviation within 10%. It enhances heating performance, supporting mechanized repair and intelligent oil-gas transport.

Keywords: Multi–field coupling simulation; induction heating; pipeline anti-corrosion joint repair technology; electromagnetic simulation.

1. Introduction

The development of pipeline infrastructure exhibits a distinct trend toward large diameters and thick walls [1, 2]. Against this backdrop, the traditional manual operation mode for mechanized anti-corrosion joint repair of pipelines using heat-shrinkable sleeves—encompassing core processes such as derusting, pipeline heating, coating application, and heat-shrinkable tape installation—has been increasingly inadequate in meeting the requirements of modern engineering

* Corresponding author

[1] Prof., College of Safety and Ocean Engineering, China University of Petroleum, Beijing, Changping, Beijing, 102249, China, zhu@cup.edu.cn

[2] Prof.., Key Laboratory of Oil and Gas Safety and Emergency Technology, Ministry of Emergency Management, Changping, Beijing, 102249, China, zhu@cup.edu.cn

[3] Mr., College of Mechanical and Transportation Engineering, China University of Petroleum, Beijing, Changping, Beijing, 102249, China cxdu268@163.com

[4] Dr., College of Mechanical and Transportation Engineering, China University of Petroleum, Beijing, Changping, Beijing, 102249, 2022310309@student.cup.edu.cn

[5] Prof., College of Mechanical and Transportation Engineering, China University of Petroleum, Beijing, Changping, Beijing, 102249, smzhang@cup.edu.cn

for construction efficiency, repair quality, and automation level. There is an urgent need for high-efficiency technical solutions tailored to this specific scenario.

Induction heating technology, endowed with advantages such as rapid heating and excellent controllability, has achieved multi-dimensional breakthroughs in relevant research fields. In terms of optimizing heating uniformity and local precision, scholars have developed a regulatory system characterized by "overall optimization + local precision control" through approaches including the improvement of magnetic conductor structures [3, 4] and the application of magnetized ring technology [5], which have respectively enhanced the overall heating uniformity and controlled the local heating error within 10%. In the realm of multi-physics coupling simulation and engineering applications, technologies such as coupled models based on partial differential equations [6, 7], simplified methods using surface impedance formulas [8], optimization via the conjugate gradient method [9], and thermal analysis models for magneto-thermal systems [10] have realized the dual improvement of computational accuracy and efficiency, providing robust technical support for process optimization. Regarding innovations in coil design, studies on dual-coil topology [11], parameter optimization of spiral coils [12], flexible liquid-metal coils [13], and magnetic field models of rectangular coils [14] have expanded the application scenarios and adaptability of coils. Additionally, achievements such as the simplification of magnetic field equations [15], full-coupled multi-field simulation [16], quantification of heat generation mechanisms [17], coupling system [18], establishment of an induction coil speed-peak temperature threshold correlation model [19], and derivation of heat transfer laws from steel plate temperature analysis and extensive induction heating experiments [20] have further deepened the understanding of induction heating mechanisms and consolidated the theoretical foundation for engineering practice.

Currently, induction heating technology has been extensively applied in fields such as metallurgy, medicine, and military [21-27]. However, significant deficiencies persist in research targeting the anti-corrosion joint repair of pipelines, with three core limitations: first, the lack of a magneto-thermal coupling simulation system tailored to the demands of pipeline anti-corrosion joint repair, coupled with the absence of systematic analysis on the optimization of key process parameters (e.g., operating frequency, heating distance) and their impacts on heating performance; second, previous studies have predominantly focused on the improvement of individual technical links, failing to address the requirement for multi-process integration in anti-corrosion joint repair.

The research objectives of this paper are as follows: 1) Developing an integrated equipment integrating derusting, induction heating, and automatic spraying to realize the synchronous operation of multiple processes and improve

the automation level of anti-corrosion repair; 2) Quantitatively optimizing key parameters such as heating distance and frequency to meet the precise temperature control requirements of anti-corrosion joint repair; 3) Verifying the adaptability of the equipment under extreme initial temperatures ranging from -20°C to 22°C through simulations, ensuring its reliability in practical working conditions.

The remaining sections of this paper are organized as follows. Section 2 presents the design scheme of the multifunctional pipeline anti-corrosion joint repair equipment, technical parameters of induction heating, and key formula derivations. Section 3 introduces the multi-field simulation system and analyzes the induction heating results under different ambient temperatures and parameter conditions. Finally, conclusions are drawn in Section 4.

2. Methods

2.1 Technical requirements for pipeline heating

Based on engineering practice, the following technical specifications are established for the equipment:

- Pipe Specification: Applicable to pipelines with a nominal diameter of 1016 mm and a working pipe end width of 400 mm.
- Temperature Requirement: Achieve average temperature rise ⩾200°C.
- Heating Uniformity: Ensure temperature deviation across pipeline measurement points ⩽10% of the average temperature.
- Heating Duration: Complete the heating process within 200s.The chapter titles will be numbered, written in small letters, 12 pts, bold, left aligned, as above.

2.2 Multifunctional equipment system scheme design

The presentation will be clear and concise, and the symbols used therein will be specified in a symbol list (if necessary). The International System of Units will be used. There will be no apparatus or installation descriptions.

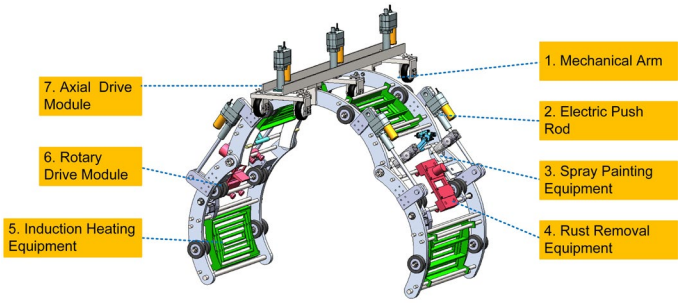

Fig. 1. Structural schematic of the equipment

Figure 1 illustrates the equipment structure, comprising an axial drive module, three mounting frames, two sandblasting rust-removal modules, four induction heating modules, two painting modules, two circumferential drive modules, and two sets of electric push rods. The mounting frames support all functional modules, with electric push rods driving their opening/closing for secure pipeline clamping. The axial drive module's three equidistant electric push rods connect to drive wheels for longitudinal movement. Symmetric sandblasting modules enable 360° descaling, while four evenly distributed induction heating modules heat synchronously during sandblasting to shorten cycles. Symmetric painting modules spray primer post-heating, and circumferential drive modules at frame ends provide rotational force for coordinated rust removal, heating, and painting.

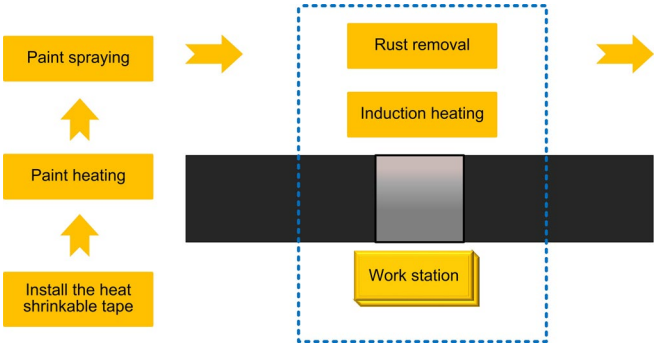

Fig. 2. Process flow diagram of the equipment

Figure 2 shows the workflow: the equipment is hoisted onto the pipeline via lifting tools, moved to the work area by the axial drive module through drive wheel set lifting/lowering, then clamped tightly by electric push rods. It rotates circumferentially for simultaneous rust removal and induction heating, followed by automatic painting, before moving to the next zone. This enables continuous automation.

The equipment boasts high integration and automation, with concurrent rust removal and heating. Automated painting cuts processing time, ensures consistent heat-shrinkable sleeve anti-corrosion joint repair quality, and reduces manual safety hazards.

2.3 Derivation of electromagnetic field formulas

This paper investigates the heating performance of induction heating coils. It optimizes the coil-pipeline distance and analyzes the existing module's heating effect via electromagnetic field simulations, while studying its performance under different initial temperatures through magneto-thermal coupling simulations.

Per Faraday's electromagnetic induction principle, induced current requires a "closed conductor loop" and an "alternating magnetic field". The studied pipe, with good electrical conductivity and structural integrity, acts as an annular closed conductor, fully meeting the physical conditions for induced current generation.

With reference to the relevant literature [28-32], In the entire heating device, the pipe body and heating coil can be simplified as a series circuit, where the equivalent resistance and equivalent inductance in the circuit are R_S and L_S .According to Kirchhoff's Second Law (KVL), the solving equation can be derived as follows:

$$R_s = R_1 + \frac{\omega^2 M^2 L_2}{\left(R_2^2 + \omega^2 L_2^2\right)^2} \tag{1}$$

$$L_s = L_1 - \frac{\omega^2 M^2 L_2}{\left(R_2^2 + \omega^2 L_2^2\right)^2} \tag{2}$$

Where R_1 denotes the coil eesistance (Ω), L_1 is the equivalent inductance (H), ω is the equivalent inductances (Hz), M represents the mutual inductance coefficient, R_2 is the pipe eesistance. L_2 is pipe inductance.

It can be derived from the above formulation that the value of the equivalent resistance is greater than its original value. The underlying reasons can be analyzed as follows: primarily, both eddy current losses and hysteresis losses consume power, leading to an increase in the equivalent resistance; furthermore, the magnitude of the operating frequency can also alter the value of the equivalent resistance.

From the formulas for equivalent resistance and inductance, the power factor of the load can be derived, and its expression is as follows:

$$\cos\Phi_L = \frac{R_s}{\sqrt{R_s^2 + (\omega L)^2}} \tag{3}$$

Where Φ_L denotes the power factor of the load.

Its active power and reactive power are respectively as follows:

$$P_L = I_1^2 \omega R_s \tag{4}$$

$$Q_L = I_1^2 \omega L_s \tag{5}$$

It can be seen from the above two formulas that factors such as operating frequency, the distance between the pipe body and the coil, and material properties all exert an influence on the load. By analyzing the conditions under which these factors affect the impedance, effective measures can be adopted to improve the heating efficiency.

The heating effect of the induction heating coil on the pipe body is determined by the heating power at each individual point on the pipe body. The heating power P at a point on the pipe body reflects the heating capacity of that specific point, which is given by the following expression:

$$P = i_1^2 R_2 \tag{6}$$

According to Faraday's Law of Electromagnetic Induction, the magnitude of the induced electromotive force (emf) in a circuit is proportional to the rate of change of the magnetic flux passing through that circuit.

$$\varepsilon = \frac{d\Phi}{dt} \tag{7}$$

ε is the induced electromotive force (emf) of the pipeline.

The eddy current generated is expressed as follows:

$$i_2 = \frac{\varepsilon}{R_2} = \frac{S}{R_2}\frac{dB}{dt} \tag{8}$$

Where S denotes the Pipe body area (m^2), B is the Magnetic induction intensity at the pipe body (T).

As a conductive medium, the pipeline is exposed to an alternating magnetic field generated by the induction coil's sinusoidal current, inducing an electromotive force that drives eddy currents and resistive heating. Thus, the pipeline and coil can be modeled as a series circuit. To calculate the magnetic induction intensity at any point P on the pipeline, the heating coil geometry shown in Figure 3 is theoretically simplified to a circular loop. This "circular equivalence" greatly reduces computational complexity; moreover, the central magnetic field of non-circular coils differs minimally from circular ones, with controllable errors ensuring result reliability.

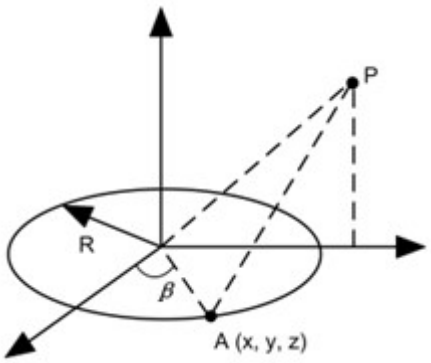

Fig. 3. Heating simplified model

From the Biot–Savart law, the following formula can be obtained:

$$B = \frac{\mu_0}{4\pi}\oint\frac{i_l d_l r}{r^3} = \frac{\mu_0 i_l R}{4\pi}\int_0^{2\pi}\frac{zi\cos\beta + zj\sin\beta + R\left(\cos\beta - \sin\beta\right)k}{\left(x^2 + y^2 + z^2 - 2R\cos\beta - 2yR\sin\beta\right)^{3/2}}dB \quad (9)$$

Where μ_0 denotes the vacuum permeability, B is the Magnetic flux density, R is the Edge radius (m), β represents the Direction angle. using numerical analysis to calculate and solve, the simplified expression for the magnetic induction intensity at the heating point of the pipe body is:

$$B = \frac{\mu_0 i_l \cos\theta}{4\pi d}\beta \quad (10)$$

Where d denotes the distance between the heating point and the heating coil(m), θ is the angle between the tangent direction of the magnetic line of force and the normal line of the tube body, i_l is Eddy current. Due to the rotational motion of the heating module around the pipeline over time, the circumferential non–uniformity of pipeline heating is minimized. Therefore, the radial distance between the induction heating module and the pipeline surface becomes a critical parameter governing the heating performance, as it directly influences eddy current distribution and heat generation efficiency.

3. Simulation and analysis

3.1. Parameter settings

A DN1016 pipeline model with four heating modules was built in SolidWorks, imported into Maxwell's transient simulation module. Excitation sources were applied to induction coil cross-sections (5000 Hz), with four cross-sections' current excitations specified as:

$$I(t) = 500\cdot\sin(2\pi\cdot 5000\cdot t) \quad (11)$$

Material properties (including skin depth and electrical conductivity) were selected from the software library. Each heating module has 6 copper coils, with other parameters configured per engineering specifications. To replicate real conditions, a rotation point was defined at the pipeline's end-face centroid, with the parameterized rotation angle (step size 6.6s) invoking the preset dataset via "pwlx(ds1, time)". For Maxwell's transient module, an appropriate time step and 200s total duration balance accuracy and computational efficiency.

3.2. Electromagnetic Simulation Analysis of the Induction Heating System

Through solving the parameterized model in Maxwell software, the spatial distribution of magnetic induction intensity within the computational domain is obtained. Figure 4 presents the magnetic induction intensity distribution diagram.

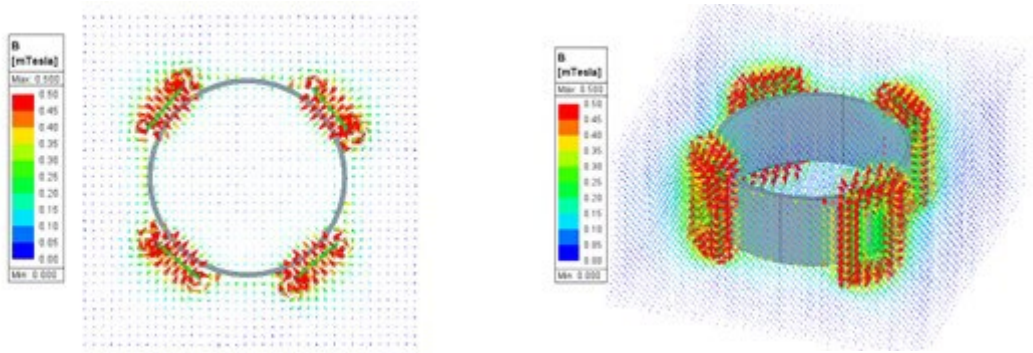

(a) (b)

Figure. 4. Magnetic flux density distribution. (a) magnetic induction intensity distribution map in the default direction; (b) magnetic induction intensity distribution map in the planar direction

The magnetic induction intensity distribution aligns with the induction heating coil configuration. Proximity to the coil exhibits densely packed magnetic field lines and relatively high magnetic induction intensity, while regions distant from the coil show a gradual decrease in intensity. To further characterize the heating performance and quantify the surrounding magnetic induction intensity, three measurement points are selected on the coil to monitor intensity variations at each point under different phase angles. Figure 5 illustrates the magnetic induction intensity distribution across the selected points.

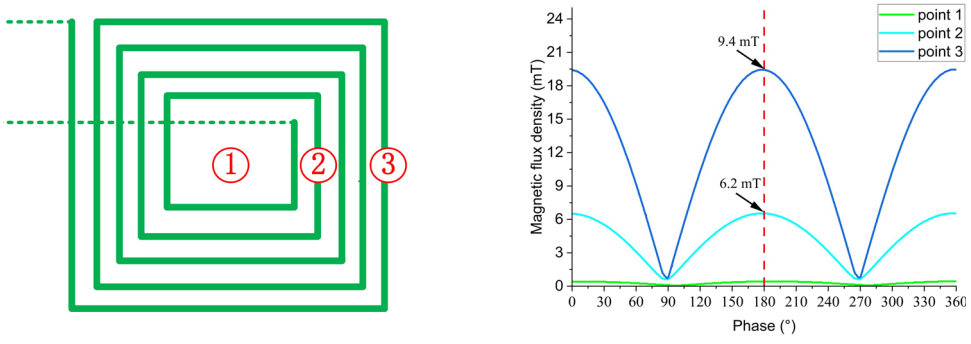

(a) (b)

Figure. 5. Magnetic induction intensity distribution at selected points. (a) schematic of measurement positions; (b) magnetic induction intensity distribution curve

Figure 5 shows the magnetic induction intensity for three measurement points: the green curve (Point 1) indicates lower intensity at the coil's central axis due to symmetrical magnetic field distribution. The blue curve (Point 2) displays obvious fluctuations in magnetic induction intensity with phase angle changes, featuring an amplitude of approximately 6.2 mT, while the red curve (Point 3)

shows significant oscillations with an amplitude of around 19.4 mT. Different distances between the induction heating coil and the pipeline surface leads to varying eddy current distributions and heat generation in the tube, prompting simulations for multiple spacing configurations. In the transient thermal module, the Maxwell–imported load represents core loss values; with 15 iterations in Maxwell, the core loss curve stabilizes. Keeping conductivity and permeability constant, the coil–to–pipeline distance was altered, and Table 2.1 lists core loss values for different heating distances.

Table 1

Coreloss values for different heating distances

Distance (mm)	electric current (A)	Work frequency (Hz)	Coreloss (W)	decline rate (%)
3	500	5000	36453	/
4	500	5000	34976	4.0
5	500	5000	32452	4.3
6	500	5000	29164	9.8
7	500	5000	25360	15.9
8	500	5000	19980	21.1

The distance between the heating module and the pipeline largely determines the effect of induction heating. Table 1 shows that the smaller the distance, the larger the core loss value, that is, the more obvious the heating effect. On the other hand, as the distance increases, the core loss value also decreases more rapidly. Especially when the distance is greater than 5mm, the decline rate rapidly increases from 10% to 21.1%. Due to the structure of the equipment, the distance needs to be greater than or equal to 3mm. Therefore, the distance between the heating module and the pipeline is set to 3mm during simulation.

After the electromagnetic simulation is completed, import the heat generation results generated by the electromagnetic simulation in Maxwell into the transient heat module in Workbench to conduct a heating simulation of the pipeline.

3.3. Magnetothermal Coupling Simulation Analysis of the Pipeline

- Temperature increase situation

The thermal load calculated by Maxwell software is imported into the transient thermal analysis module of Workbench for simulation. This study conducts induction heating simulations on pipelines under varying initial temperatures.

The heating duration was set to 200s, with the heat transfer coefficient specified as 20 W/m^2 for the pipeline's outer surface and 10 W/m^2 for the inner surface. Other boundary conditions were configured as required prior to model solution. Simulations were executed under diverse initial temperature

environments. The average temperature rise profiles for four operational scenarios with initial temperatures of 22°C, 8°C, –6°C, and –20°C were exported. Figure 8 illustrates the comparative temperature rise curves across the four temperature conditions.

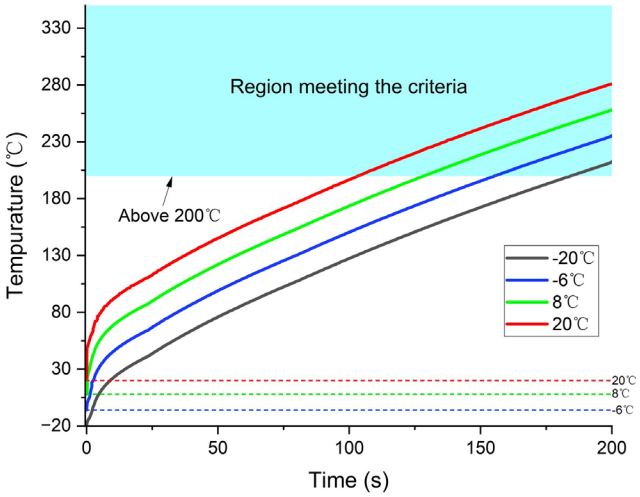

Figure. 6. Comparison of average temperature rise of four different initial temperatures

Figure 6 illustrates a strong consistency in the temperature rise curves across different initial temperature conditions, demonstrating that the induction heating system maintains excellent adaptability under varying ambient temperature environments.

- Comparison of different working frequencies

In engineering applications involving large–diameter pipeline workpieces, the induction heating frequency typically ranges between 1 kHz and 20 kHz. Given that the heating temperature required for the operating conditions in this study is moderate and higher working frequencies would lead to increased energy consumption, the induction heating frequency was optimized. A total of seven groups of different frequencies were selected for comparative analysis. With the initial temperature set to –20°C and a heating duration of 200s, all other parameters were kept constant during the simulations.

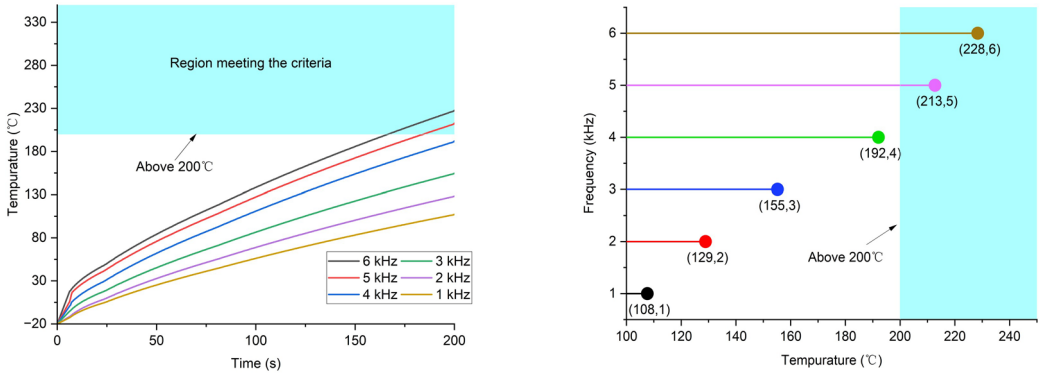

(a) (b)

Figure. 7. Pipeline temperature comparison at different frequencies. (a) temperatures after 200s heating at different frequencies; (b) temperature curves during 200s heating at different frequencies

Figure 7 (a) depicts the temperatures of the pipeline after 200s heating at different frequencies. In the frequency range of 3–4 kHz, frequency variations exhibit the most significant impact on temperature rise, with an approximate 19.3% increase in temperature. When the frequency reaches 5 kHz, the effect of frequency changes on temperature rise diminishes, resulting in a 6.5% temperature increase. Frequencies above 5 kHz enable the heating temperature to meet the operating condition requirements. Compared to the commonly used 3 kHz frequency in engineering, the temperature rise at 5 kHz within 200s is approximately 27.2%, ensuring both heating requirements and energy efficiency. Figure 7 (b) illustrates the temperature curves during 200s heating at different frequencies. At 1–3 kHz, the relatively large skin depth leads to uniform heat distribution on the steel pipe, resulting in a gentle temperature rise curve. In the 4–6 kHz range, the skin effect becomes more pronounced, causing rapid temperature increase in the initial stage and a steeper slope in the temperature curve.

- Heating uniformity

Based on the four distinct initial temperatures described earlier, 48 measurement points are strategically selected on the pipeline for local temperature assessment. Figure 8 illustrates the point arrangement methodology. Along the pipeline axis, transverse planes are established at 200mm intervals. On each plane, within a circular cross–section with a diameter of 1016 mm, 16 equally spaced points are distributed for temperature sampling.

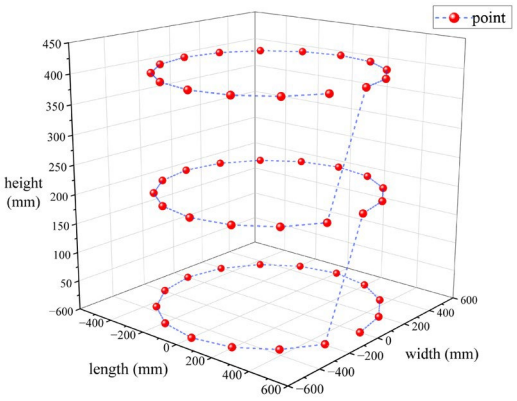

Figure. 8. The position of the temperature measurement points on the pipe body

To characterize the spatial temperature distribution, transverse sections are taken at 200mm intervals along the pipeline's longitudinal axis, with 16 circumferentially distributed points on each section (within the 1016mm diameter cross–section). The figure illustrates how initial temperatures of 22°C, 8°C, -6°C, and –20°C influence the local temperature elevation at each point, highlighting both axial and circumferential thermal gradients induced by the induction heating process. This dataset enables a detailed analysis of heating uniformity and thermal response consistency across diverse ambient conditions.

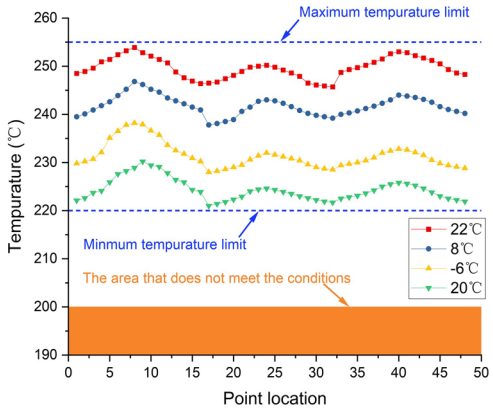

Figure. 9. Temperature conditions at various points with different initial temperatures

Figure 9 presents the temperature rise profiles of 48 measurement points on the pipeline after 200s of heating under different initial temperature conditions. Induction heating demonstrates remarkable temperature uniformity, evidenced by the consistent heating performance across all 48 selected measurement points. After 200s of heating, each point achieved temperatures exceeding 200°C, underscoring the reliability of the heating process. The specific temperature

ranges for different initial conditions are as follows: when the initial temperature was 22°C, the 16 measurement points recorded temperatures fluctuating between 240–260°C; at an initial temperature of 8°C, the temperature readings spanned from 235–255°C; with an initial temperature of -6°C, the measured temperatures ranged within 225–245°C; and when the initial temperature was set at – 20°C, the temperature values were observed to vary from 215–235°C.

Statistical analysis shows that in all cases, the maximum local temperature deviation from the average does not exceed 10%—even at the extreme initial temperature of -20°C. This narrow deviation confirms induction heating's excellent overall temperature uniformity for the pipeline. In terms of heat transfer mechanism, induction heating generates heat directly inside the pipeline via electromagnetic induction, achieving more uniform heating than external conduction-based methods. Specifically, its alternating magnetic field ensures relatively uniform distribution of eddy currents (the core heat source) across the pipeline's cross-section and axially, minimizing local hotspots and cold spots.

Furthermore, under the four different initial temperature conditions, the deviations in the temperature rise curves of each measurement point exhibit significant consistency. This phenomenon can be explained from two aspects: On one hand, the cylindrical geometry of the pipeline possesses inherent symmetry, which guides the stable and regular diffusion of heat in the circumferential and axial directions. This prevents local heat accumulation or dissipation caused by structural asymmetry, keeping the temperature deviation of each measurement point within a specific range and providing a structural basis for the consistency of deviations. On the other hand, the structural design and magnetic field distribution characteristics of the induction coil ensure that the electromagnetic effect exerted on each position of the pipeline during induction heating maintains high consistency. Even with variations in initial temperature, the heating law of each measurement point remains uniform, ultimately contributing to the consistent characteristic of temperature deviations.

4. Conclusions

This study focuses on the anti-corrosion joint repairing scenario of large-diameter pipelines. Based on magnetothermal coupling simulation technology, it analyzes the induction heating performance, and breaks through the limitations of pure experiments in "large-diameter pipeline heating" and "extreme initial temperature simulation" via computational modeling, providing theoretical and technical support for efficient heating in anti-corrosion joint repairing.

To elaborate on the simulation verification results, all research objectives have been fully achieved: Regarding the objective of "developing integrated equipment integrating rust removal, induction heating, and automatic spraying," the designed integrated anti-corrosion joint repairing equipment realizes the

synchronization of multiple processes, markedly improving the automation level. For the objective of "quantitatively optimizing key process parameters," Maxwell electromagnetic simulation was employed to optimize the "module-pipeline" distance—when the distance is reduced from 5 mm to 3 mm, the heating capacity is increased by 19.9%. Additionally, the heating efficiency at a working frequency of 5 kHz is confirmed to be 1.7 times that at 3 kHz, meeting the demand for precise temperature control. Concerning the objective of "verifying adaptability to extreme initial temperatures," Workbench transient thermal coupling simulation results show that under operating conditions of 22°C, 8°C, -6°C, and -20°C, the average temperature of the DN1016 pipeline exceeds 200°C after 200 s of heating, with a temperature deviation of $\leqslant 10\%$ among 48 measuring points, ensuring reliability in practical working conditions.

This study has three key limitations: First, simulation assumes constant electromagnetic and thermal conductivity of pipeline materials, ignoring temperature-induced dynamic property changes (e.g., reduced magnetic permeability of some metals at high temperatures), which may cause deviations under extreme high-temperature conditions. Second, it excludes pipeline surface interference factors (e.g., rust degree, anti-corrosion coating thickness variations in practical engineering), potentially altering local electromagnetic induction efficiency and temperature uniformity. Third, the research is limited to DN1016 pipelines and specific initial temperatures, without exploring adaptability to small-diameter or non-circular cross-section pipelines, restricting conclusion applicability.

Future research will address these limitations: establish a dynamic "material property-temperature" model to integrate temperature’s influence on electromagnetic and thermophysical parameters, improving extreme-condition prediction accuracy; expand pipeline surface state analysis (e.g., rust grade, coating type) and quantify impacts on heating efficiency via experiments; extend research objects (small-diameter and special-shaped pipelines) and frequency ranges (1-10 kHz high-frequency heating laws), and modify the model using industrial on-site data to enhance multi-scenario engineering applicability.

At present, the field of pipeline anti-corrosion joint repairing is gradually developing towards the integration of "automation + digital simulation". The simulation method and equipment design idea of this study can provide a reference for the technological upgrading in this field, and the subsequent in-depth research to overcome the limitations will further promote the accurate application of induction heating technology in industrial pipeline anti-corrosion.

REFERENCES

[1] L. Guangyue and L. Zhao, "Gas migration laws and nitrogen injection rate optimization in the commissioning process of large-diameter gas pipes in the Russia-China eastern route pipeline project," *Natural Gas Industry,* vol. 40, no. 9, pp. 123-130, 2020.

[2] W. Zeng *et al.*, "Quality analysis and flow measurement technologies for natural gas of the China–Russian Eastern Gas Pipeline," *Nat. Gas Ind,* vol. 40, pp. 111-119, 2020.

[3] V. Nemkov, R. Goldstein, and V. Bukanin, "Optimal design of internal induction coils," *Heat Treating Progress,* vol. 5, no. 6, pp. 85-89, 2005.

[4] V. Nemkov, R. Goldstein, and R. Ruffini, "Magnetic flux controllers for induction heating applications," in *Transactions of Materials and Heat Treatment Proceedings of the 14th IFHTSE congress*, 2004, vol. 25, no. 5.

[5] L. Bao, B. Wang, X. You, H. Li, Y. Gu, and W. Liu, "Numerical and experimental research on localized induction heating process for hot stamping steel sheets," *International Journal of Heat and Mass Transfer,* vol. 151, p. 119422, 2020.

[6] H. Liu and J. Rao, "Notice of Retraction: Numerical Simulation of Oil Steel Pipe in Induction Heat Treatment Process," in *2010 Second International Workshop on Education Technology and Computer Science*, 2010, vol. 2: IEEE, pp. 174-177.

[7] H. Liu and J. Rao, "Coupled modeling of electromagnetic-thermal problem in induction heating process considering material properties," in *2009 International Conference on Information Engineering and Computer Science*, 2009: IEEE, pp. 1-4.

[8] J. Nerg and J. Partanen, "A simplified FEM based calculation model for 3-D induction heating problems using surface impedance formulations," *IEEE transactions on magnetics,* vol. 37, no. 5, pp. 3719-3722, 2002.

[9] Y. Favennec, V. Labbé, and F. Bay, "Induction heating processes optimization a general optimal control approach," *Journal of computational physics,* vol. 187, no. 1, pp. 68-94, 2003.

[10] A. Plait, T. de Larochelambert, S. Giurgea, and C. Espanet, "Experimental validation of a multiphysics modeling for a magnetocaloric bench," *Applied Thermal Engineering,* vol. 211, p. 118415, 2022.

[11] S. Pattanapichai, T. Jansaengsuk, and J. Thongsri, "A dual coil induction heating machine for jewelry factories developed by electromagnetic analysis," *Journal of Advanced Joining Processes,* vol. 7, p. 100146, 2023.

[12] M. Patil, R. K. Choubey, and P. K. Jain, "Influence of coil shapes on temperature distribution in induction heating process," *Materials Today: Proceedings,* vol. 72, pp. 3029-3035, 2023.

[13] L.-X. Cao, T. Yin, M.-X. Jin, and Z.-Z. He, "Flexible circulated-cooling liquid metal coil for induction heating," *Applied Thermal Engineering,* vol. 162, p. 114260, 2019.

[14] C. Xu, W. Zheng, Y. Wang, X. Zhou, and Z. Li, "Green and recyclable demolition of steel reinforced concrete: Application and calculation model of induction heating demolition technology," *Journal of Building Engineering,* vol. 61, p. 105304, 2022.

[15] D. Hömberg, "A mathematical model for induction hardening including mechanical effects," *Nonlinear Analysis: Real World Applications,* vol. 5, no. 1, pp. 55-90, 2004.

[16] W. Elsaady, C. Moughton, and A. Nasser, "Coupled numerical modelling and experimental analysis of domestic induction heating systems," *Applied Thermal Engineering,* vol. 227, p. 120170, 2023.

[17] X. Fu, M. Ma, S. Wang, C. Teng, and W. Liang, "Heat generation and transfer simulation of a high temperature heat pipe under induction heating based on a coupled model," *Applied Thermal Engineering,* vol. 232, p. 121025, 2023.

[18] K. Gao, X. Qin, Z. Wang, S. Zhu, and Z. Gan, "Effect of magnetizer geometry on the spot induction heating process," *Journal of materials processing technology,* vol. 231, pp. 125-136, 2016.
[19] J. Wang, B. Yi, C. Zhang, H. Zhou, and Y. Shu, "Experiments of double curvature plate bending with induction heating and processing parameters investigation by computational analysis," *Ocean Engineering,* vol. 192, p. 106596, 2019.
[20] S.-g. Fu, "The Numerical Analysis of Induction Heating Furnace Temperature Field," in *2009 International Conference on Computational Intelligence and Software Engineering*, 2009: IEEE, pp. 1-5.
[21] M.-H. Ahn, S.-K. Baek, J. Min, and J.-H. Park, "A portable electromagnetic induction heating device for point-of-care diagnostics," *BioChip Journal,* vol. 10, pp. 208-214, 2016.
[22] C. Gu, S. Zou, T. Qu, J. Ling, and Z. Han, "Design of HTS coil for magnetic driving spacecraft," *IEEE Transactions on Applied Superconductivity,* vol. 20, no. 3, pp. 997-1000, 2010.
[23] U.-M. Jow and M. Ghovanloo, "Geometrical design of a scalable overlapping planar spiral coil array to generate a homogeneous magnetic field," *IEEE transactions on magnetics,* vol. 49, no. 6, pp. 2933-2945, 2012.
[24] X. Liu and S. Hui, "Optimal design of a hybrid winding structure for planar contactless battery charging platform," *IEEE Transactions on Power Electronics,* vol. 23, no. 1, pp. 455-463, 2008.
[25] E. Plumed, I. Lope, and J. Acero, "Modeling and design of cookware for induction heating technology with balanced electromagnetic and thermal characteristics," *IEEE Access,* vol. 10, pp. 83793-83801, 2022.
[26] P. Guillén, H. Sarnago, J. Acero, J. M. Burdío, S. Llorente, and Ó. Lucía, "Induction Heating Appliances: Fifty Years of Technological Success: Paving the Path for Sustainable Homes," *IEEE Industrial Electronics Magazine,* 2025.
[27] Y. Wang, X. Hu, M. Jiang, J. Wang, M. Wei, and L. Zhang, "Temperature field characterization and optimization of temperature field distribution in pipe lining process based on electromagnetic induction heating system," *Case studies in thermal engineering,* vol. 28, p. 101609, 2021.
[28] V. Davydova, A. Shcherbinin, M. Naumov, and S. Ershov, "A Numerical Study on Induction-Resistive Electric-Heating Processes of Pipelines," *Russian Electrical Engineering,* vol. 92, no. 11, pp. 668-671, 2021.
[29] I. Makulov, P. Vasilyev, and R. Khazieva, "Modeling of the Induction Heating Process of a Pipeline for Industrial Equipment," in *2024 Dynamics of Systems, Mechanisms and Machines (Dynamics)*, 2024: IEEE, pp. 1-5.
[30] F. Zhou, Q. Cheng, H. Zhao, Z. Zhang, and H. Wang, "Flowing Heating System for Pipeline of Electromagnetic Coupling of Power Frequency Without the Iron Core and Its Structure Optimization," *Journal of Energy Resources Technology,* vol. 146, no. 4, p. 041702, 2024.
[31] Y. Zhu and Y. Luo, "A simplified heat source model for thick plate bending via high-frequency induction line heating," *Ships and Offshore Structures,* vol. 14, no. 1, pp. 64-73, 2019.
[32] A. V. Serikov, "Thermal Simulation in Transformer Type Heating Devices," in *Current Problems and Ways of Industry Development: Equipment and Technologies*: Springer, 2021, pp. 587-596.